Engineering Analysis with Boundary Elements 159 (2024) 418–433

Contents lists available at ScienceDirect

Engineering Analysis with Boundary Elements

journal homepage: www.elsevier.com/locate/enganabound

NURBS-boundary-based quadtree scaled boundary finite element method study for irregular design domain

Xinqing Li [a], Hailiang Su [a,b], Jianghong Yang [a], Guifeng Gao [a], Yingjun Wang [a,*]

[a] National Engineering Research Center of Novel Equipment for Polymer Processing, The Key Laboratory of Polymer Processing Engineering of the Ministry of Education, Guangdong Provincial Key Laboratory of Technique and Equipment for Macromolecular Advanced Manufacturing, South China University of Technology, Guangzhou 510641, China

[b] Commercial Vehicle Technology Center, Dongfeng Liuzhou Automobile Co., LTD, Liuzhou 545005, China

ARTICLE INFO

Keywords:
SBFEM
Quadtree decomposition
NURBS-based-boundary
Irregular design domain

ABSTRACT

The traditional finite element analysis for irregular design domains often encounters challenges such as intricate mesh discretization and inaccurate boundary description. In this paper, we propose a quadtree scaled boundary finite element method based on NURBS curves where the boundaries can be accurately represented. Quadtree decomposition, which satisfies the 2:1 rule, is employed to rapidly subdivide the analysis domain. The scaled boundary finite element method (SBFEM) is utilized to analyze the internal elements and address the displacement incompatibility issue of hanging nodes in the quadtree. Furthermore, the boundary element is discretized into boundary curves and internal lines, whose displacement fields are respectively constructed by the NURBS shape functions and the Lagrange shape functions, and then the subsequent analysis of the boundary element is completed by SBFEM. Finally, numerical examples are tested to demonstrate the feasibility of the proposed method, which effectively enhances computational efficiency and accuracy in solving irregular design domains.

1. Introduction

As a numerical method in computational mechanics, the finite element method (FEM) exhibits remarkable versatility and extensive applicability. However, the pre-processing stage of finite element analysis, which includes mesh discretization and element construction among other processes, can be quite time-consuming [1]. Furthermore, due to its inherent limitations as an approximate numerical solution, the FEM is not suitable for accurately characterizing the boundary of irregular design domains [2]. In 1997, Wolf and Song [3] pioneered the scaled boundary finite element method (SBFEM), which ingeniously combines the FEM with the boundary element method (BEM). This method preserves the features of low computational dimensionality and absence of fundamental solutions, thereby paving a new avenue for engineering scientific computation that demands high efficiency and accuracy.

In recent years, the combination of quadtree decomposition and SBFEM has emerged as a prominent research area. Quadtree, as a two-dimensional geometric adaptive mesh generation technique based on hierarchical tree structures [4,5], enables efficient mesh subdivision. It is a customary practice to limit the maximum difference in the division levels between two adjacent elements to 1 (2:1 rule [6,7]), that is, to satisfy the balance. Balanced quadtree mesh can reduce the types of quadtree elements to 6, thereby mitigating computational complexity and facilitating a rapid and seamless transition of element size. However, quadtree mesh is seldom employed in conventional finite element frameworks due to the presence of hanging nodes and the fitting of curved boundary [8]. In 2014, Man et al. [9] proposed a novel scaled boundary finite element method utilizing a quadtree mesh composed of higher-order elements. In particular, the generation of the quadtree mesh is fully automated, greatly simplifying user input and operational steps, while SBFEM can effectively overcome the limitations of the quadtree mesh. Ooi et al. [10–12] presented a hybrid quadtree SBFEM (HQSBFEM) that integrates quadtree mesh with polygons featuring an arbitrary number of sides, as shown in Fig. 1, and incorporated polygons directly modeled by SBFEM on the boundary to significantly enhance the accuracy of boundary modeling. On this basis, an efficient heavy mesh algorithm combining quadtree decomposition and simple Boolean operation was explored to simulate crack propagation. Song et al. [13] investigated an adaptive refinement strategy based on quadtree SBFEM.

* Corresponding author.
E-mail address: wangyj84@scut.edu.cn (Y. Wang).

https://doi.org/10.1016/j.enganabound.2023.12.007
Received 31 October 2023; Received in revised form 23 November 2023; Accepted 5 December 2023
Available online 16 December 2023
0955-7997/

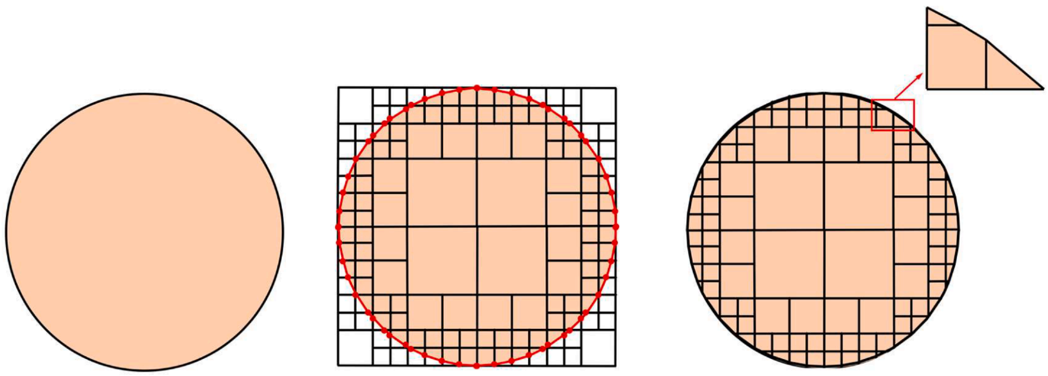

Fig. 1. Decomposition diagram of hybrid quadtree SBFEM.

Chen et al. [14] utilized SBFEM based on quadtree polygons in the modeling calculation of functionally graded materials, which significantly enhanced computational efficiency. Yu et al. [15] applied the HQSBFEM to two-dimensional transient heat transfer problems, systematically verifying the effectiveness and stability of the method in solving models with complex geometries. Additionally, references [16–19] discussed the image-based quadtree SBFEM, which provided robust theoretical and practical support for efficiently and accurately solving irregular design domains.

Furthermore, Isogeometric analysis (IGA) [20] offers an appealing alternative approach for efficiently solving irregular design domains. The essence of IGA lies in the concept of isoparametric, where the basis functions employed for accurate geometric modeling are also utilized as the foundation for numerical method solution spaces [21]. Non-uniform rational B-splines (NURBS), a commonly used geometric spline in IGA, possess a unique property of maintaining high-order continuity on the element interface [22], which is an exceptional feature that traditional high-order finite element basis functions lack. Zhang et al. [23] were the first to utilize NURBS to describe the boundaries of SBFEM and subsequently proposed a novel numerical method known as scaled boundary isogeometric analysis (SBIGA) [24]. Klinkel et al. [2] developed a NURBS-based hybrid collocation-Galerkin method that combined the advantages of both SBFEM and isogeometric collocation method. Zang et al. [25] proposed a NURBS-enhanced SBFEM method that inserted NURBS curves into the divided polygonal mesh boundaries to examine the heat transfer problem in anisotropic media. Recently, a NURBS-enhanced finite element analysis method based on scale boundary parameterization was proposed [26], which organically combined the NURBS basis function and the Lagrange basis function to describe the boundary of curve elements. Additionally, the utilization of NURBS in SBFEM has been extended to investigate various problems including fracture mechanics [27], electrostatics [28], seepage [29], and soil vibration [30]. The majority of the aforementioned studies, however, are based on artificially divided NURBS patches or given detailed initial NURBS information, which inevitably poses challenges when applied to the analysis of complex design domains.

On this basis, we propose a NURBS-boundary-based quadtree scaled boundary finite element method (NQSBFEM) for irregular design domains. The curve boundary of the design domain is described by NURBS, which achieves accurate representation without requiring a substantial quantity of seed points for detailed division of the domain boundary, thereby reducing mesh division costs. Among them, quadtree decomposition following the 2:1 rule is utilized to mesh the design domain. Under the given NURBS information, the knot vector corresponding to the intersection point of the curve and quadtree mesh is obtained through point inversion, followed by knot insertion to obtain updated NURBS information. This results in the NURBS control points being precisely located at the intersection position, facilitating subsequent accurate solutions. By means of SBFEM, the boundary elements are discretized into NURBS curves and internal lines. Subsequently, the displacement fields of both are constructed using NURBS shape functions and traditional Lagrange shape functions respectively, enabling efficient analysis and solution.

The outline of the remainder of this paper is as follows: Section 2 reviews the underlying concepts of NURBS and SBFEM; Section 3 presents an innovative implementation approach for NQSBFEM; Section 4

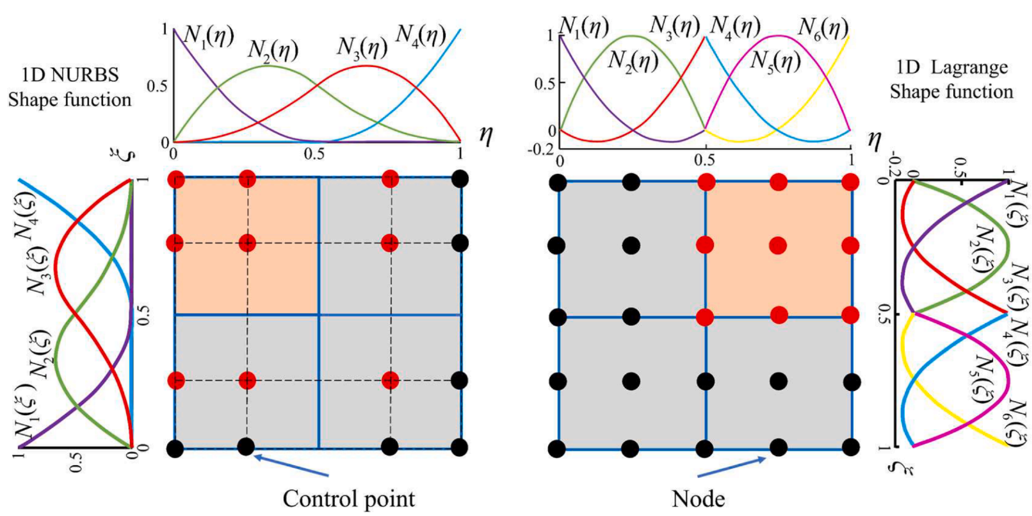

Fig. 2. Comparison of NURBS and Lagrange shape functions in 1D.

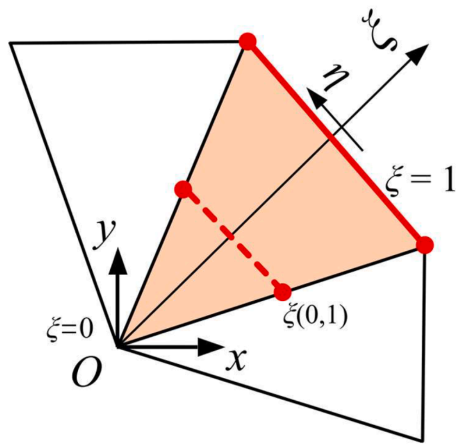

Fig. 3. Scaled boundary coordinate system.

elaborates the flow of NQSBFEM implementation; Numerical examples are presented in Section 5 to demonstrate the effectiveness of the proposed method; and finally, Section 6 briefly summarizes the key points discussed throughout this paper.

2. Summary of basic theories

2.1. Concepts of NURBS

Currently, various spline techniques are utilized in IGA, such as hybrid B-splines and NURBS [31,32], T-splines [33], PHT splines [34], etc. However, B-splines and NURBS remain the most prevalent spline techniques for IGA. Non-uniform rational B splines (NURBS), a common method for generating and representing curves and surfaces, can be constructed using B-splines. In B-spline, the knot vector $\Xi = \{\eta_0, \eta_1, \cdots, \eta_{n+p}\}$ is defined as a sequence of non-decreasing real numbers in the parameter space, where n represents the number of basis functions (equivalent to the number of control points) and p denotes the order of the B-spline, with a maximum multiplicity of the knot vector being $p+1$.

In a one-dimensional space, the B-spline basis functions under a given knot vector can be recursively defined using the well-known Cox-de Boor formula [35]

$$
\begin{aligned}
B_{i,0}(\eta) &= \begin{cases} 1, \text{if } \eta_i \le \eta < \eta_{i+1} \\ 0, \textit{Otherwise} \end{cases} \\
B_{i,p}(\eta) &= \frac{(\eta-\eta_i)B_{i,p-1}(\eta)}{\eta_{i+p}-\eta_i} + \frac{(\eta_{i+p+1}-\eta)B_{i+1,p-1}(\eta)}{\eta_{i+p+1}-\eta_{i+1}} \text{if } \eta_i \le \eta < \eta_{i+1}
\end{aligned}
\tag{1}
$$

where, we define the convention $0/0 = 0$. The B-spline basis function can map the points in the parameter space where the knot vectors are located to the physical space where the control points are located, thus realizing the correspondence between the knot span $[\eta_i, \eta_{i+1})$in the parameter space and the element V^i in the physical space.

Furthermore, the NURBS basis functions can be implemented through B-splines rationalization. By assigning a positive weight w_i to each B-spline basis function, the NURBS basis function is defined as

$$N_{i,p}(\eta) = \frac{B_{i,p}(\eta)w_i}{\sum_j^n B_{j,p}(\eta)w_j} \tag{2}$$

Compared with the conventional Lagrange shape functions, as depicted in Fig. 2, the NURBS basis functions possess numerous distinctive properties [36], which are succinctly enumerated as follows: (1) Nonnegativity: $N_{i,p} \ge 0$; (2) Partition of unity: $\sum_i^n N_{i,p}(\eta) = 1$; (3) Local support: $N_{i,p}(\eta) = 0$ for $\eta \notin [\eta_i, \eta_{i+p+1})$;(4) Differentiability: $N_{i,p}(\eta)$ is p - k times differentiable where k is the multiplicity of the knots.

The corresponding NURBS curve can be expressed as

$$C(\eta) = \sum_{i=0}^{n} N_{i,p}(\eta)\boldsymbol{P}_i \tag{3}$$

where $\boldsymbol{P}_i$ is the control point of the NURBS curve.

2.2. Concepts of SBFEM

For the fundamental concepts and coordinate transformations of the SBFEM, Wolf and Song have provided a detailed discussion in the literatures [37,38], and only a concise overview is given in this section. For the coordinate transformation of the scaled boundary, a two-dimensional region has been selected as the subject of analysis, which is illustrated in Fig. 3. Where O is referred as scaling center, (ξ, η) represents scaled boundary coordinate system. The conversion from the Cartesian coordinate system to the scaled boundary coordinate system is achieved by

$$
\begin{aligned}
\widehat{x}(\xi,\eta) &= x_0 + \xi \boldsymbol{N}^u(\eta)\boldsymbol{x} = x_0 + \xi x(\eta) \\
\widehat{y}(\xi,\eta) &= y_0 + \xi \boldsymbol{N}^u(\eta)\boldsymbol{y} = y_0 + \xi y(\eta)
\end{aligned}
\tag{4}
$$

where $\boldsymbol{N}^u$ represents the finite element shape functions, defined as $\boldsymbol{N}^u = [N_1^u\ N_2^u] = [(1-\eta)/2\ (1+\eta)/2]$, $(\widehat{x}, \widehat{y})$ represents the coordinate of arbitrary point in the physical domain, $(\boldsymbol{x}, \boldsymbol{y})$ denotes the nodal coordinates, defined as $\boldsymbol{x} = [x_1, x_2]^{\mathrm{T}}, \boldsymbol{y} = [y_1, y_2]^{\mathrm{T}}$, (x_0, y_0) and $(x(\eta), y(\eta))$ denote the scaling center's physical coordinate and the physical coordinates of points on the boundary corresponding to the tangential coordinate η, respectively.

The displacements $\boldsymbol{u}(\xi, \eta) = [u_x(\xi, \eta)\ u_y(\xi, \eta)]^{\mathrm{T}}$ are interpolated as

$$\boldsymbol{u}(\xi,\eta) = \boldsymbol{N}_u(\eta)\boldsymbol{u}(\xi) \tag{5}$$

where $\boldsymbol{N}_u$ represents the interpolation functions, defined as $\boldsymbol{N}_u = [N_1^u \boldsymbol{I}_{2\times2}\ N_2^u \boldsymbol{I}_{2\times2}]$, $\boldsymbol{I}_{2\times2}$ is the identity matrix, $\boldsymbol{u}(\xi)$ represents analytic components in the radial direction, defined as $\boldsymbol{u}(\xi) = [u_{1x}(\xi,\eta)\ u_{1y}(\xi,\eta)\ u_{2x}(\xi,\eta)\ u_{2y}(\xi,\eta)]^{\mathrm{T}}$. By introducing the strain equation ($\boldsymbol{\varepsilon} = \boldsymbol{L}^{\mathrm{T}}\boldsymbol{u}$), the expression for strain can be derived

$$\boldsymbol{\varepsilon}(\xi,\eta) = \boldsymbol{B}_1(\eta)\boldsymbol{u}(\xi)_{,\xi} + \frac{1}{\xi}\boldsymbol{B}_2(\eta)\boldsymbol{u}(\xi) \tag{6}$$

where

$$
\begin{aligned}
\boldsymbol{B}_1(\eta) &= \boldsymbol{b}_1(\eta)\boldsymbol{N}_u(\eta) = \frac{1}{|\boldsymbol{J}|}\begin{bmatrix} y(\eta)_{,\eta} & 0 \\ 0 & -x(\eta)_{,\eta} \\ -x(\eta)_{,\eta} & y(\eta)_{,\eta} \end{bmatrix}\boldsymbol{N}_u(\eta) \\
\boldsymbol{B}_2(\eta) &= \boldsymbol{b}_2(\eta)\boldsymbol{N}_u(\eta)_{,\eta} = \frac{1}{|\boldsymbol{J}|}\begin{bmatrix} -y(\eta) & 0 \\ 0 & x(\eta) \\ x(\eta) & -y(\eta) \end{bmatrix}\boldsymbol{N}_u(\eta)_{,\eta}
\end{aligned}
\tag{7}
$$

where $\boldsymbol{J}$ is the Jacobi matrix, expressed as

$$\boldsymbol{J} = \begin{bmatrix} x(\eta) & y(\eta) \\ x(\eta)_{,\eta} & y(\eta)_{,\eta} \end{bmatrix} \tag{8}$$

Therefore, the stress expression is

$$\boldsymbol{\sigma}(\xi,\eta) = \boldsymbol{D}\left(\boldsymbol{B}_1(\eta)\boldsymbol{u}(\xi)_{,\xi} + \frac{1}{\xi}\boldsymbol{B}_2(\eta)\boldsymbol{u}(\xi)\right) \tag{9}$$

Substituting the aforementioned coordinate transformation into the principle of virtual work, we can elegantly transform the control partial differential equations into a set of second-order ordinary differential equations pertaining to the scaled boundary coordinates $\xi\xi$, that is, scaled boundary finite element equation

$$\boldsymbol{E}_0\xi^2\boldsymbol{u}(\xi)_{,\xi\xi} + \left(\boldsymbol{E}_0 + \boldsymbol{E}_1^{\mathrm{T}} - \boldsymbol{E}_1\right)\xi\boldsymbol{u}(\xi)_{,\xi} - \boldsymbol{E}_2\boldsymbol{u}(\xi) = 0 \tag{10}$$

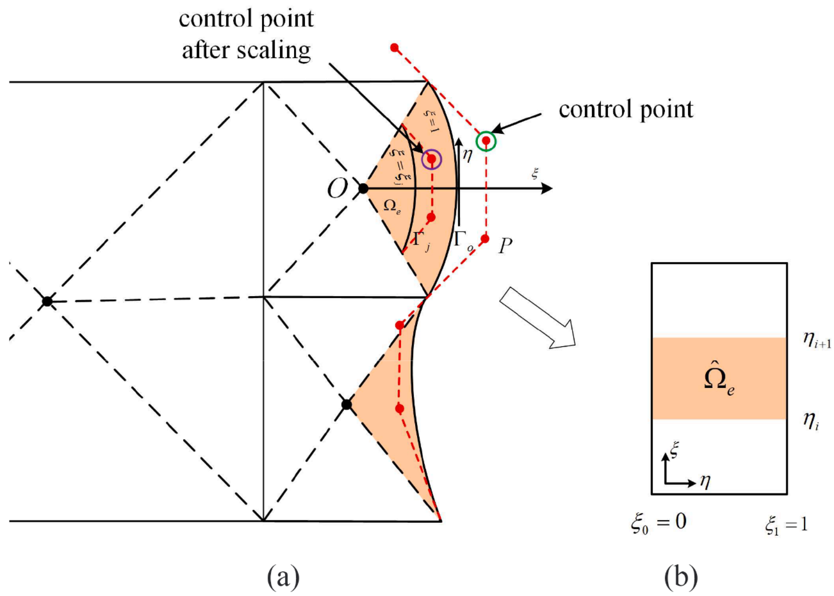

Fig. 4. Schematic diagram of boundary element based on NURBS, (a) model diagram, (b) parameter space.

where the coefficient matrix $\boldsymbol{E}_0$, $\boldsymbol{E}_1$ and $\boldsymbol{E}_2$ can be represented as follows

$$\begin{aligned}\boldsymbol{E}_0 &= \int_{\partial\Omega} \boldsymbol{B}_1(\eta)^{\mathrm{T}} \boldsymbol{D} \boldsymbol{B}_1(\eta) |\boldsymbol{J}| \mathrm{d}\eta \\ \boldsymbol{E}_1 &= \int_{\partial\Omega} \boldsymbol{B}_2(\eta)^{\mathrm{T}} \boldsymbol{D} \boldsymbol{B}_1(\eta) |\boldsymbol{J}| \mathrm{d}\eta \\ \boldsymbol{E}_2 &= \int_{\partial\Omega} \boldsymbol{B}_2(\eta)^{\mathrm{T}} \boldsymbol{D} \boldsymbol{B}_2(\eta) |\boldsymbol{J}| \mathrm{d}\eta\end{aligned} \tag{11}$$

Assume that the general solution of the SBFEM equation has a power series of the following form:

$$\boldsymbol{u}(\xi) = c_1 \xi^{\lambda_1} \boldsymbol{\phi}_1 + c_2 \xi^{\lambda_2} \boldsymbol{\phi}_2 + \ldots + c_n \xi^{\lambda_n} \boldsymbol{\phi}_n = \boldsymbol{\phi} \xi^{\lambda} \boldsymbol{c} \tag{12}$$

where λ_i and ϕ_i are the corresponding eigenvalue and eigenvector respectively, and the integral constant c_i depends on the boundary conditions. Visually, this solution can be interpreted as a modal superposition method that is similar to the standard finite element format. The eigenvalue vector can be regarded as the modal displacement vector of the boundary node, and eigenvalue is the radial modal scale factor.

By substituting the general solution into the SBFEM equation of displacement, the following quadratic eigenvalue equation is obtained:

$$\left(\lambda^2 \boldsymbol{E}_0^2 - \lambda\left(\boldsymbol{E}_1^{\mathrm{T}} - \boldsymbol{E}_1\right) - \boldsymbol{E}_2\right)\boldsymbol{\phi} = 0 \tag{13}$$

$$\boldsymbol{q} = \left(\boldsymbol{E}_1^{\mathrm{T}} - \lambda \boldsymbol{E}_0\right)\boldsymbol{\phi} \tag{14}$$

where Eq. (14) represents a modal interpretation of the boundary force, and can be considered as the nodal force mode required for the corresponding displacement mode on the equilibrium boundary. Therefore, all quantities related to ϕ are assumed to be general solutions associated with displacement, while q is directly linked to modal forces at the boundary.

It has been demonstrated that linearization of the above quadratic equations is beneficial at the cost of doubling the number of equations to be solved. Subsequently, the following formula is derived

$$\boldsymbol{Z}\begin{bmatrix}\boldsymbol{\phi} \\ \boldsymbol{q}\end{bmatrix} = \lambda \begin{bmatrix}\boldsymbol{\phi} \\ \boldsymbol{q}\end{bmatrix} \tag{15}$$

where $\boldsymbol{Z}$ is the Hamilton matrix, defined as

$$\boldsymbol{Z} = \begin{bmatrix} -\boldsymbol{E}_0^{-1}\boldsymbol{E}_1^{\mathrm{T}} & \boldsymbol{E}_0^{-1} \\ \boldsymbol{E}_2 - \boldsymbol{E}_1\boldsymbol{E}_0^{-1}\boldsymbol{E}_1^{\mathrm{T}} & \boldsymbol{E}_1\boldsymbol{E}_0^{-1} \end{bmatrix} \tag{16}$$

It can be obtained by schur decomposition [39]

$$\boldsymbol{Z}\begin{bmatrix}\boldsymbol{\phi} \\ \boldsymbol{q}\end{bmatrix} = \lambda \begin{bmatrix}\boldsymbol{\phi} \\ \boldsymbol{q}\end{bmatrix} = \begin{bmatrix}\boldsymbol{\phi}_1 & \boldsymbol{\phi}_2 \\ \boldsymbol{q}_1 & \boldsymbol{q}_2\end{bmatrix}\begin{bmatrix}\boldsymbol{\lambda}^- & \\ & \boldsymbol{\lambda}^+\end{bmatrix} \tag{17}$$

where the superscript "+" and "−" represent the positive and negative eigenvalues respectively.

To determine the stiffness matrix of the domain, the eigenvalues and eigenvectors are brought into the general solution

$$\boldsymbol{u}(\xi) = \boldsymbol{\phi}_1 \xi^{\lambda^+} \boldsymbol{c}_1 + \boldsymbol{\phi}_2 \xi^{\lambda^-} \boldsymbol{c}_2 \tag{18}$$

For the bounded domain problem, the second part of Eq. (18) can be omitted. Additionally, to determine the stiffness matrix in the finite domain, the displacement $u(\xi = 1)$ at the boundary is compared with its corresponding equivalent nodal force$\boldsymbol{P} = \boldsymbol{q}_1\boldsymbol{c}_1$. Since the integration constant imposes a boundary condition on the force mode, the integration constant $\boldsymbol{c}_1$ is determined by calculating the value of Eq. (18) at $\xi = 1$.

$$\boldsymbol{c}_1 = \boldsymbol{\phi}_1^{-1}\boldsymbol{u}(\xi = 1) \tag{19}$$

Subsequently, substitute the aforementioned equation into the expression denoting the corresponding nodal force $\boldsymbol{P}$

$$\boldsymbol{P} = \boldsymbol{q}_1\boldsymbol{\phi}_1^{-1}\boldsymbol{u}(\xi = 1) \tag{20}$$

Therefore, the stiffness matrix of the bounded domain is

$$\boldsymbol{K} = \pm \boldsymbol{q}_1\boldsymbol{\phi}_1^{-1} \tag{21}$$

3. NURBS-boundary-based quadtree SBFEM

3.1. Scaled boundary element based on NURBS

For the irregular design domain, the boundary is represented by a NURBS curve. Additionally, the boundary element is discretized into boundary curve and internal line elements with the SBFEM, as depicted in Fig. 4. The radial coordinate ξ and the tangential coordinate η constitute a scaled boundary coordinate system, with the latter constructing into the NURBS curve parameter space of the outer boundary. And the radial coordinate is a dimensionless scale parameter that represents the "scale factor" of the outer boundary, exerting control over the shape and extent of the domain. When $\xi = 1$, it represents the outer

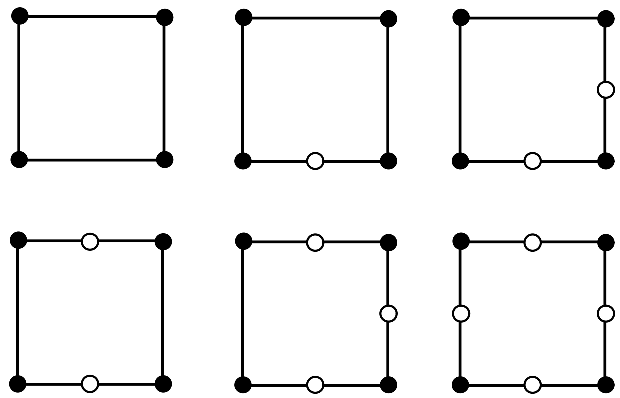

Fig. 5. Internal element forms.

boundary Γ_o; when $\xi = \xi_j$, it indicates the scaled boundary Γ_j; and when $\xi = 0$, it denotes the scaling center O. The NURBS curved edges of the boundary elements in physical space are transformed into parameter space segments$[\eta_i, \eta_{i+1})$ through mapping. Consequently, the boundary domain Ω_e is also mapped onto a corresponding parameter space segment, where $\xi_1 = 1$, $\xi_0 = 0$.

For the internal elements within the design domain, there are a total of 16 distinct element configurations, six of which are illustrated in Fig. 5. The remaining elements can be obtained by rotating from the following set of element forms [40]. Where black circles and white circles represent element nodes and hanging nodes, respectively. Furthermore, the stiffness matrices of the aforementioned elements are pre-computed and stored in memory for quick retrieval during the solution process.

3.2. Point inversion

From Fig. 4, it can be observed that the control points are not situated at element nodes, which unavoidably impacts the accuracy of the solution. To ensure the accuracy of subsequent SBFEM analysis for NURBS curves of boundary elements, a control point application strategy is proposed, that is, the coincidence of control points and element nodes is controlled by point inversion and knot insertion. Where, the element nodes (the intersection point of the quadtree mesh and NURBS curve $\boldsymbol{C}(\eta)$) located on the NURBS boundary of physical space are utilized for inversion to obtain the corresponding knot vector.

In the context where the node is defined as $\boldsymbol{P}_{\text{in}} = (x, y, z)$ determining the corresponding parameter $\overline{\eta}$ such that $\boldsymbol{C}(\overline{\eta}) = \boldsymbol{P}_{\text{in}}$ is referred as point inversion. The solution process can be divided into three steps: (1) Utilizing the strong convex hull property of NURBS curves, identify which spans of the curve $\boldsymbol{C}(\eta)$ can possibly contain node $\boldsymbol{P}_{\text{in}}$; (2) Employing knot refinement or insertion to extract the aforementioned spans and convert them into power basis form; (3) For each span, determine three polynomial equations with unknown parameters, and if these equations have a common solution, then $\boldsymbol{P}_{\text{in}}$ is located on the curve $\boldsymbol{C}(\eta)$.

Suppose that degree $p = 2$, then a span $\boldsymbol{r}(\eta)$ of NURBS curve can be represented as vector function

$$\boldsymbol{r}(\eta) = \boldsymbol{a}_0^w + \boldsymbol{a}_1^w \eta + \boldsymbol{a}_2^w \eta^2 \tag{22}$$

where $\boldsymbol{a}_i^w = (w_i x_i, w_i y_i, w_i z_i, w_i)$. Projecting the above equation into 3D space and setting it equal to $\boldsymbol{P}_{\text{in}}$, we obtain

$$\begin{aligned} \frac{w_2 x_2 \eta^2 + w_1 x_1 \eta + w_0 x_0}{w_2 \eta^2 + w_1 \eta + w_0} &= x \\ \frac{w_2 y_2 \eta^2 + w_1 y_1 \eta + w_0 y_0}{w_2 \eta^2 + w_1 \eta + w_0} &= y \\ \frac{w_2 z_2 \eta^2 + w_1 z_1 \eta + w_0 z_0}{w_2 \eta^2 + w_1 \eta + w_0} &= z \end{aligned} \tag{23}$$

which yields

$$\begin{aligned} w_2(x_2 - x)\eta^2 + w_1(x_1 - x)\eta + w_0(x_0 - x) = 0 \\ w_2(y_2 - y)\eta^2 + w_1(y_1 - y)\eta + w_0(y_0 - y) = 0 \\ w_2(z_2 - z)\eta^2 + w_1(z_1 - z)\eta + w_0(z_0 - z) = 0 \end{aligned} \tag{24}$$

It should be noted that this paper solely focuses on the 2D scenario, thus letting $z = 0$. Additionally, the Newton iteration method is employed to minimize the distance between $\boldsymbol{P}_{\text{in}}$ and $\boldsymbol{C}(\eta)$, as illustrated in Fig. 6. If the minimum distance falls below a predetermined precision, then the point is deemed to lie on the curve.

Given an initial value η_0, define the dot product

$$f(\eta) = \boldsymbol{C}'(\eta) \cdot (\boldsymbol{C}(\eta) - \boldsymbol{P}_{\text{in}}) \tag{25}$$

Regardless of whether $\boldsymbol{P}_{\text{in}}$ lies on the curve, when $f(\eta) = 0$, the distance from point $\boldsymbol{P}_{\text{in}}$ to $\boldsymbol{C}(\eta)$ is minimized. Let η_i denote the parameter value obtained in the i th iteration

$$\eta_{i+1} = \eta_i - \frac{f(\eta_i)}{f'(\eta_i)} = \eta_i - \frac{\boldsymbol{C}'(\eta_i) \cdot (\boldsymbol{C}(\eta_i) - \boldsymbol{P}_{\text{in}})}{\boldsymbol{C}''(\eta_i) \cdot (\boldsymbol{C}(\eta_i) - \boldsymbol{P}_{\text{in}}) + |\boldsymbol{C}'(\eta_i)|^2} \tag{26}$$

And two zero tolerances can be employed to denote convergence, convergence criteria are as follows:

$$\begin{aligned} &|\boldsymbol{C}(\eta) - \boldsymbol{P}_{\text{in}}| \le \varepsilon_1 \\ &\frac{|\boldsymbol{C}'(\eta)(\boldsymbol{C}(\eta) - \boldsymbol{P}_{\text{in}})|}{|\boldsymbol{C}'(\eta)||\boldsymbol{C}(\eta) - \boldsymbol{P}_{\text{in}}|} \le \varepsilon_2 \\ &|(\eta_{i+1} - \eta_i)\boldsymbol{C}'(\eta)| \le \varepsilon_1 \end{aligned} \tag{27}$$

where, ε_1 indicates whether the measure of Euclidean distance is zero; ε_2 indicates whether the measure of cosine is zero.

3.3. Knot insertion

After obtaining the parameter $\overline{\eta}$ from 3.2, it is necessary to incor-

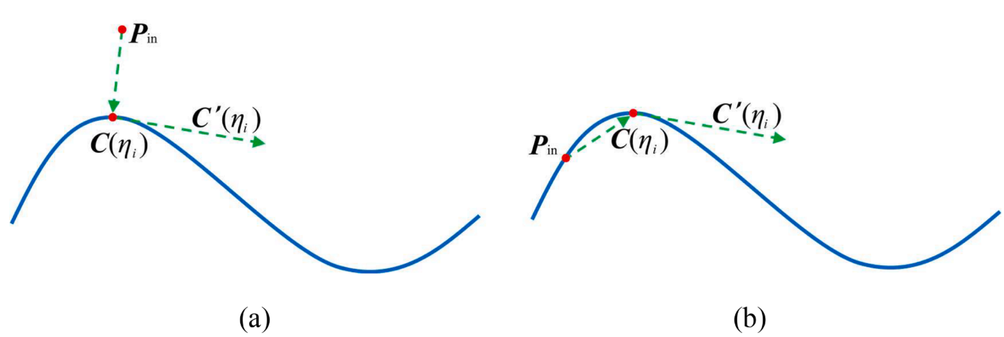

Fig. 6. (a) Projection of a point onto a curve, (b) the parameters of the point inversion.

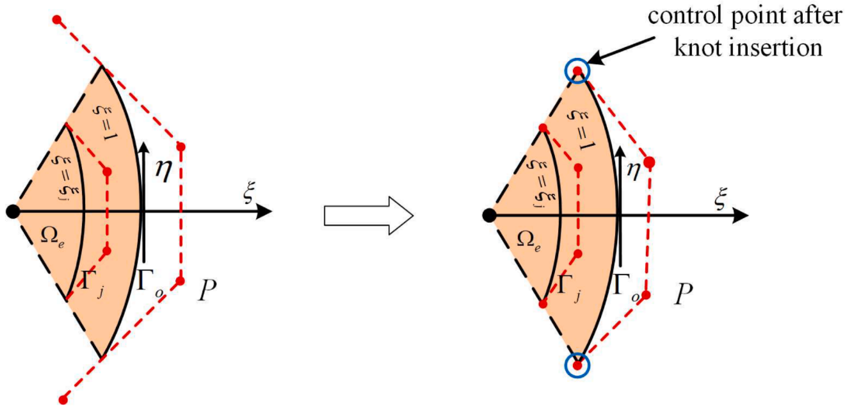

Fig. 7. Schematic diagram of the NURBS element scaled boundary model after knot insertion.

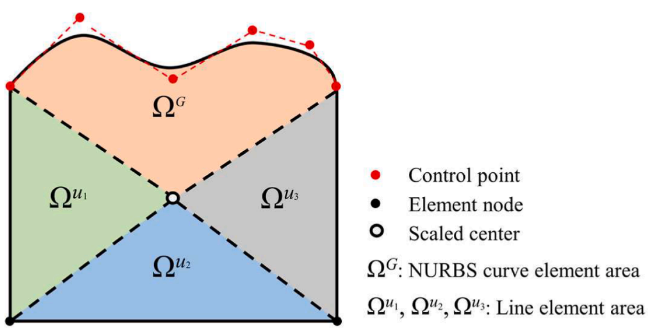

Fig. 8. Schematic diagram of boundary element.

porate it into the existing knot vector in order to construct a new knot vector and control points. Fig. 7 illustrates the schematic diagram of the NURBS element scaled boundary model after knot insertion.

Let $\overline{\eta} \in [\eta_k, \eta_{k+1})$, insert $\overline{\eta}$ into knot vector $\boldsymbol{\Xi}$ to form a new knot vector $\overline{\boldsymbol{\Xi}} = \{\overline{\eta}_0 = \eta_0, \cdots, \overline{\eta}_k = \eta_k, \overline{\eta}_{k+1} = \overline{\eta}\}$. The NURBS curve on $\overline{\boldsymbol{\Xi}}$ is represented as

$$\overline{\boldsymbol{C}}(\eta) = \sum_{i=0}^{n+1} \overline{N}_{i,p}(\eta)\boldsymbol{Q}_i \tag{28}$$

where $\overline{N}_{i,p}$ represents the basis function of p order on the knot vector $\overline{\boldsymbol{\Xi}}$, $\boldsymbol{Q}_i$ denotes the new control point, and the knot insertion can be interpreted as the solution process of $\boldsymbol{Q}_i$, which is defined as

$$\boldsymbol{Q}_i = \alpha_i \boldsymbol{P}_i + (1-\alpha_i)\boldsymbol{P}_{i-1} \tag{29}$$

where

$$\alpha_i = \begin{cases} 1, i \le k-p \\ \dfrac{\overline{\eta}-\eta_i}{\overline{\eta}_{i+p}-\eta_i}, k-p+1 \le i \le k \\ 0, i \ge k+1 \end{cases} \tag{30}$$

In actuality, the knot insertion primarily involves altering the basis of vector space, while the curve remains unchanged both geometrically and parametrically.

3.4. Solution of boundary element stiffness matrix

For quadtree decomposed design domain with NURBS-based boundaries, as mentioned above, the internal elements can be directly resolved using SBFEM. The external boundary element is depicted in Fig. 8, which can be firstly transformed into NURBS curve segments and ordinary line elements through the utilization of SBFEM.

The former, as a domain boundary, can be discretized using isogeometry, while the radial direction remains analytically treated. The mapping between physical space and parameter space can be reformulated as follow

$$\begin{aligned} \widehat{x}(\xi,\eta) &= x_0 + \eta \boldsymbol{N}(\eta)\boldsymbol{x}^{\eta} \\ \widehat{y}(\xi,\eta) &= y_0 + \eta \boldsymbol{N}(\eta)\boldsymbol{y}^{\eta} \end{aligned} \tag{31}$$

where $(\boldsymbol{x}^{\eta}, \boldsymbol{y}^{\eta})$ represents the coordinates of the control point associated with the outer boundary, $\boldsymbol{N}(\eta)$ denotes the NURBS shape functions corresponding to control points.

Using the concept of isoparametric, the displacement mode within the realm of isogeometry, namely the displacement field variable $\boldsymbol{u}^G$, can be obtained utilizing NURBS shape functions.

$$\boldsymbol{u}^G(\xi,\eta) = \boldsymbol{N}_N(\eta)\boldsymbol{u}^G(\xi) \tag{32}$$

where $\boldsymbol{N}_N = [N_1\boldsymbol{I}_{2\times2}\ N_2\boldsymbol{I}_{2\times2}\ N_3\boldsymbol{I}_{2\times2}]$ represent the shape functions $\boldsymbol{N}$, which are applied to each DOF of an element separately by means of multiplication with the identity matrix $\boldsymbol{I}_{2\times2}$.

The stress field can be mathematically formulated as

$$\boldsymbol{\sigma}(\xi,\eta) = \boldsymbol{D\varepsilon}(\xi,\eta) = \boldsymbol{D}\left(\boldsymbol{B}_1^G\boldsymbol{u}^G(\xi)_{,\xi} + \frac{1}{\xi}\boldsymbol{B}_2^G\boldsymbol{u}^G(\xi)\right) \tag{33}$$

where $\boldsymbol{B}_1^G$ and $\boldsymbol{B}_2^G$ denote the correlation between strain and displacement

$$\begin{aligned} \boldsymbol{B}_1^G &= \boldsymbol{b}_1\boldsymbol{N}_N \\ \boldsymbol{B}_2^G &= \boldsymbol{b}_2\boldsymbol{N}_{N,\eta} \end{aligned} \tag{34}$$

and

$$\begin{aligned} \boldsymbol{b}_1^G(\eta) &= \frac{1}{|\boldsymbol{J}^G|}\begin{bmatrix} \widehat{y}(\eta)_{,\eta} & 0 \\ 0 & -\widehat{x}(\eta)_{,\eta} \\ -\widehat{x}(\eta)_{,\eta} & \widehat{y}(\eta)_{,\eta} \end{bmatrix} \\ \boldsymbol{b}_2^G(\eta) &= \frac{1}{|\boldsymbol{J}^G|}\begin{bmatrix} -\widehat{y}(\eta) & 0 \\ 0 & \widehat{x}(\eta) \\ \widehat{x}(\eta) & -\widehat{y}(\eta) \end{bmatrix} \end{aligned} \tag{35}$$

where $\boldsymbol{J}^G$ is the Jacobi matrix, defined as

$$\boldsymbol{J}^G = \begin{bmatrix} \widehat{x}(\eta) & \widehat{y}(\eta) \\ \widehat{x}(\eta)_{,\eta} & \widehat{y}(\eta)_{,\eta} \end{bmatrix} \tag{36}$$

Regarding the boundary element depicted in Fig. 8, when solving its scaled boundary finite element equation, the coefficient matrix $\boldsymbol{E}_i$ ($i = 0$, 1, 2) is designated as

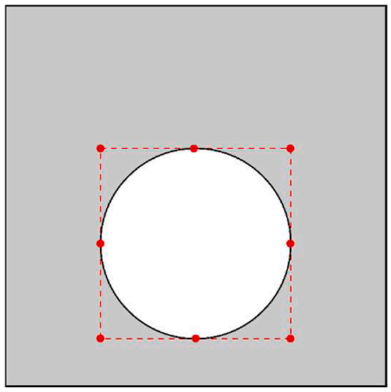

Fig. 9. Square plate with circular hole.

$$
\begin{aligned}
\boldsymbol{E}_0 &= \int_{\partial\Omega^u} \boldsymbol{B}_1(\eta)^{\mathrm{T}}\boldsymbol{D}\boldsymbol{B}_1(\eta)|\boldsymbol{J}|\mathrm{d}\eta + \int_{\partial\Omega^G} \boldsymbol{B}_1^G(\eta)^{\mathrm{T}}\boldsymbol{D}\boldsymbol{B}_1^G(\eta)|\boldsymbol{J}^G|\mathrm{d}\eta \\
\boldsymbol{E}_1 &= \int_{\partial\Omega^u} \boldsymbol{B}_2(\eta)^{\mathrm{T}}\boldsymbol{D}\boldsymbol{B}_1(\eta)|\boldsymbol{J}|\mathrm{d}\eta + \int_{\partial\Omega^G} \boldsymbol{B}_2^G(\eta)^{\mathrm{T}}\boldsymbol{D}\boldsymbol{B}_1^G(\eta)|\boldsymbol{J}^G|\mathrm{d}\eta \\
\boldsymbol{E}_2 &= \int_{\partial\Omega^u} \boldsymbol{B}_2(\eta)^{\mathrm{T}}\boldsymbol{D}\boldsymbol{B}_2(\eta)|\boldsymbol{J}|\mathrm{d}\eta + \int_{\partial\Omega^G} \boldsymbol{B}_2^G(\eta)^{\mathrm{T}}\boldsymbol{D}\boldsymbol{B}_2^G(\eta)|\boldsymbol{J}^G|\mathrm{d}\eta
\end{aligned} \tag{37}
$$

Furthermore, refer to Section 2.2 for subsequent stiffness matrix solving methods.

4. Pre-processing process

4.1. Mesh generation under NQSBFEM

This section primarily elucidates the implementation of the pre-processing process for NQSBFEM. Suppose a square plate with circular hole, as shown in Fig. 9, has a side length of 4, and the coordinates of the four corner points are [0 0; 4 0; 4 4; 0 4]. Wherein the circular hole is represented by NURBS curves with a radius of 1, the coordinates of the control points are [3 1.5; 3 0.5; 2 0.5; 1 0.5; 1 1.5; 1 2.5; 2 2.5; 3 2.5; 3 1.5], the knot vector is [0 0 0 0.25 0.25 0.5 0.5 0.75 0.75 1 1 1], and the corresponding weights are $[1\ \sqrt{2}/2\ 1\ \sqrt{2}/2\ 1\ \sqrt{2}/2\ 1\ \sqrt{2}/2\ 1]$.

Firstly, the design domain is enlarged to a specific size of $2^{10} = 1024$, while the level of largest and smallest sub-cells are taken as $2^9 = 512$ and $2^3 = 8$, respectively. Moreover, the number of seed points for the square boundary and circular hole boundary are set at 40 and 13 respectively, followed by the subsequent implementation of quadtree decomposition. The decomposed quadtree of the design domain is exhibited in Fig. 10 (a). Based on this, a balanced quadtree decomposition is performed according to the 2:1 rule, as illustrated in Fig. 10(b). It can be observed that the level difference limit between adjacent quadtree meshes after balancing does not exceed 1.

Next, proceed to label the divided mesh and accurately identify the transition blocks. The blue transition blocks correspond to the meshes where the boundary is situated, and the red dot is the intersection point where the geometric boundary intersects the blocks, as depicted in Fig. 11.

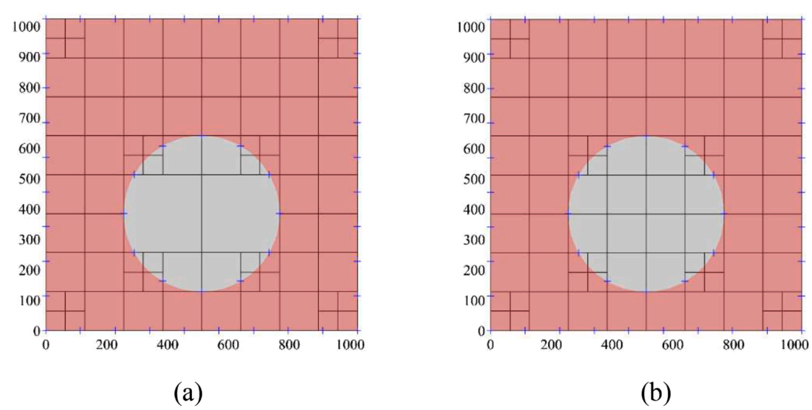

Fig. 10. Quadtree decomposition of square plate with circular hole: (a) unbalanced (b) balanced.

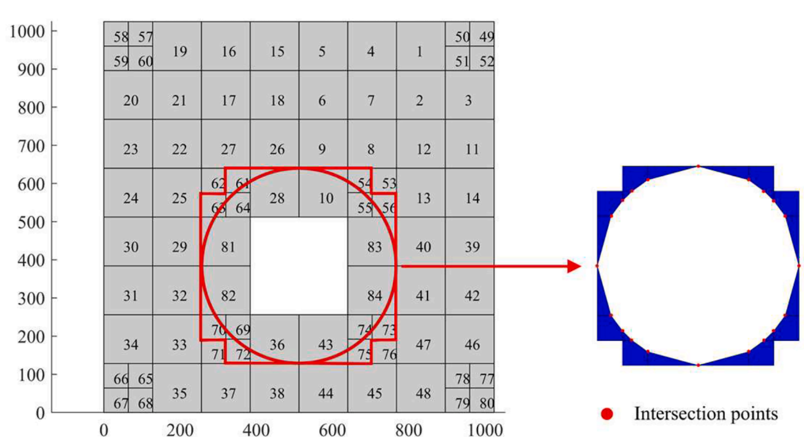

Fig. 11. Quadtree mesh and transition blocks with numbering.

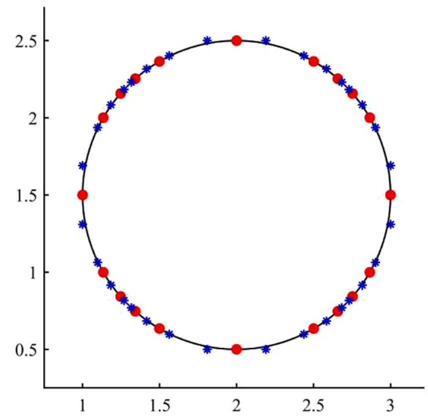

Fig. 12. The updated NURBS curve and control points.

Furthermore, it is necessary to extract the coordinates of element nodes (intersection points). On the basis of the original NURBS information, a new NURBS curve is constructed using point inversion and knot insertion as mentioned in Section 3. The updated NURBS curve is shown in Fig. 12, where red dots represent control points on boundary elements nodes and blue asterisks represent additional generated control points. It should be noted that the element nodes must be multiplied by scaling factors in order to fulfill the original size requirements. Considering that the node on the boundary connects two elements, the point inversion and knot insertion at this point will be performed twice. This will result in the occurrence of duplicate knots, thereby making the control point here being the point on the boundary.

Finally, all quadtree dimensions needs to be scaled back to original size of 4 × 4. The traditional hybrid quadtree mesh, as depicted in Fig. 13(a), exhibits a direct linear connection between nodes and nodes, which inevitably compromises the subsequent accuracy of solving. To address this issue, we replace the aforementioned linear boundaries with the updated NURBS curve to establish a new quadtree mesh, as illustrated in Fig. 13(b).

4.2. Meshes comparison under NQSBFEM and HQSBFEM

A circular structure and a petal structure with hole are used for comparison. The circular structure is formed by employing a solitary NURBS curve, whereas latter is constructed using two NURBS curves, as illustrated in Fig. 14. The basic settings of the quadtree are as follows: the size is set to $2^{10} = 1024$, the level of largest sub-cell is limit to $2^9 = 512$, and the level of smallest sub-cell is limit to $2^3 = 8$.

The circular quadtree structures under NQSBFEM and HQSBFEM are depicted in Fig. 15(a) and (b), respectively, when the number of seed point is set to 52. It can be observed that the NQSBFEM based on NURBS boundary is a viable scheme, capable of achieving a smooth boundary structure. The HQSBFEM, in contrast, displays rough boundary due to the straight-line connections between nodes.

Fig. 16(a) and (b) show the diagrams of petal quadtree structure with hole under NQSBFEM and HQSBFEM, respectively. With a seed number of 52 at the outer boundary and 10 at the inner boundary, the results demonstrate that the NQSBFEM this method is applicable for multi-boundary design domain as well. Moreover, this method yields a smoother structural boundary.

The above figures clearly demonstrate the feasibility of mesh generation under NQSBFEM. This approach enables the precise generation of smooth boundaries for structures, potentially circumventing the need

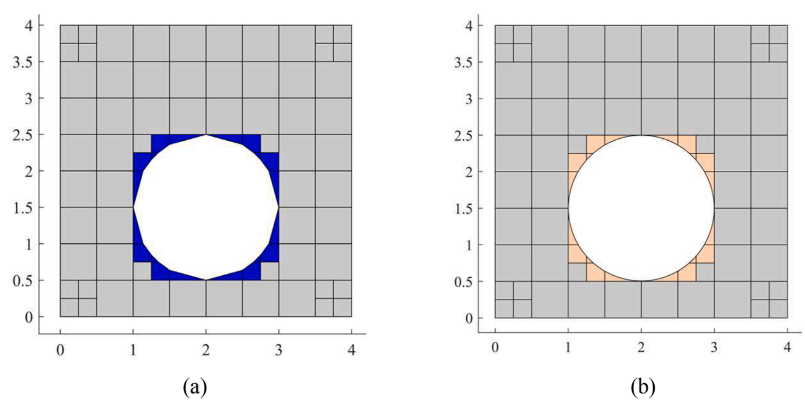

Fig. 13. Quadtree mesh after scaling, (a) HQSBFEM, (b) NQSBFEM.

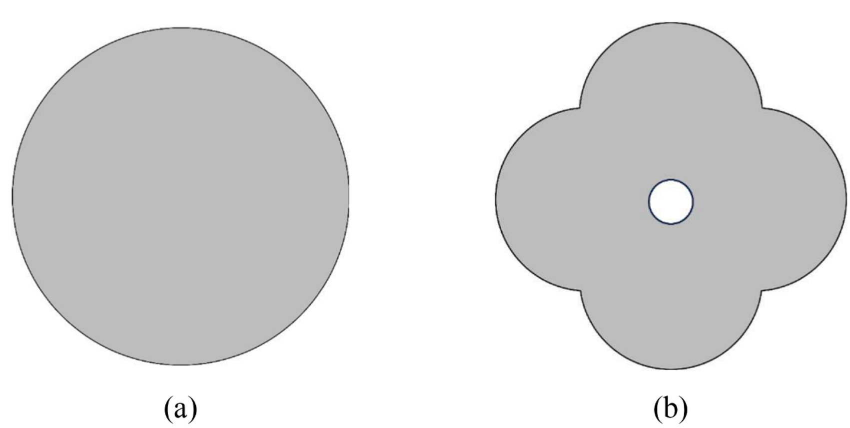

Fig. 14. Schematic diagram of structure, (a) circular, (b) petal with hole.

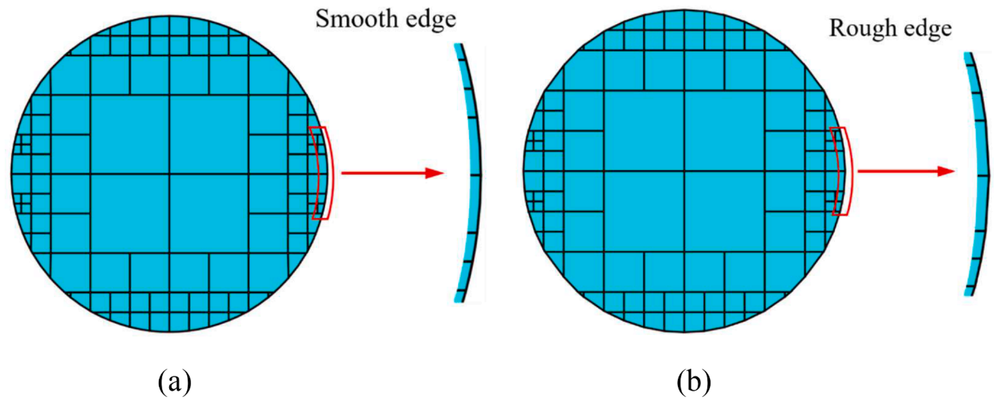

Fig. 15. Comparison of circular structures, (a) NQSBFEM, (b) HQSBFEM.

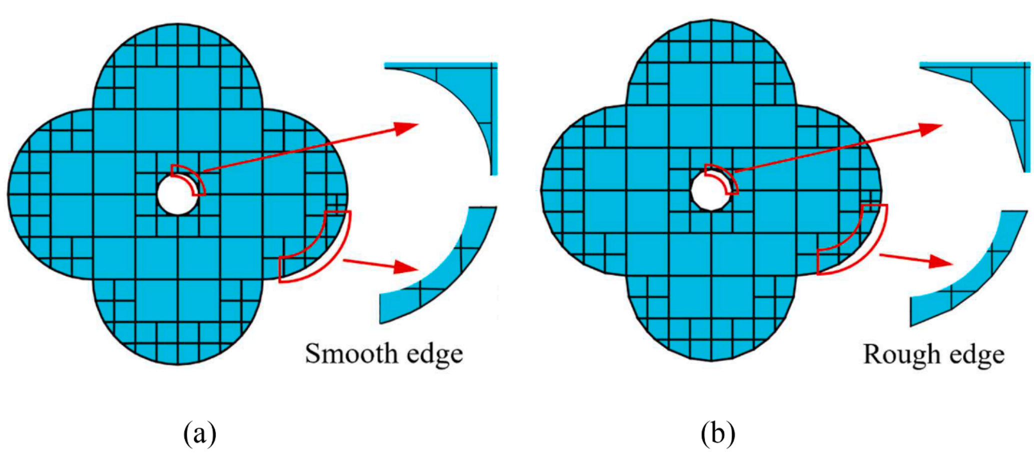

Fig. 16. Comparison of petal structures with hole, (a) NQSBFEM, (B) HQSBFEM.

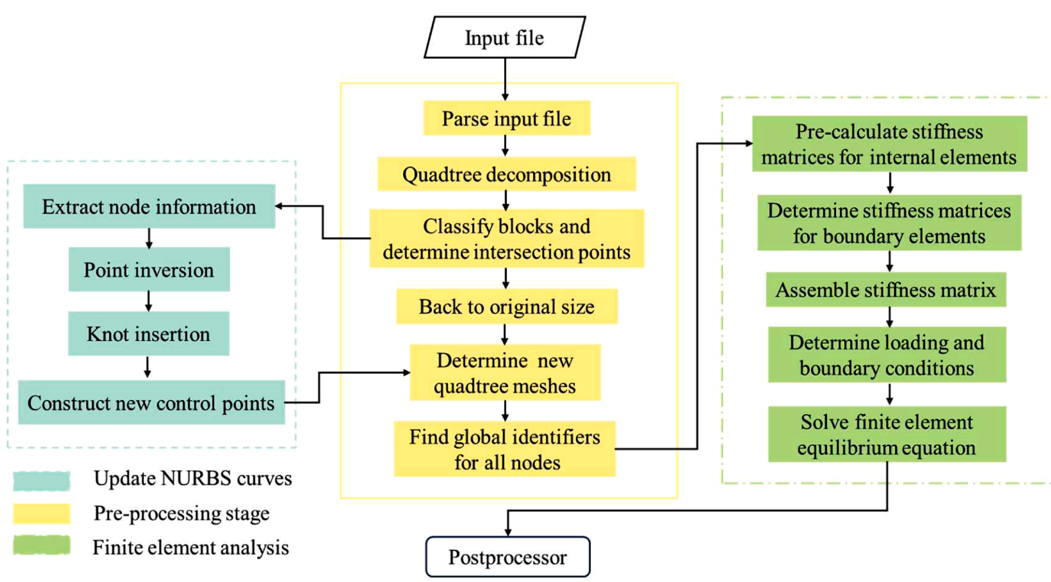

Fig. 17. Flowchart of the NQSBFEM implementation.

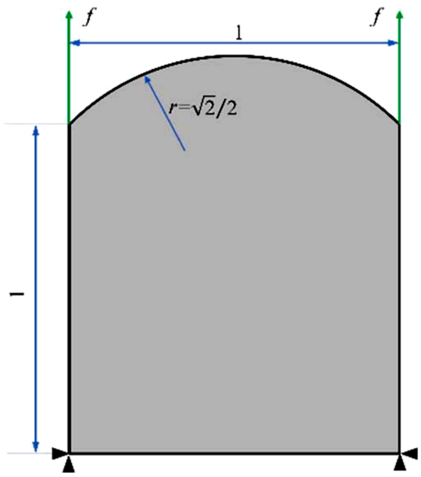

Fig. 18. Diagram of curve boundary element.

for excessive mesh refinement in traditional HQSBFEM to approximate boundary. Undoubtedly, this advancement has significant prospect to streamline mesh division processes and save valuable time.

4.3. The flowchart of NQSBFEM implementation

Firstly, defining the initial design domain, quadtree related parameters, load, boundary conditions, material properties and other information. Secondly, parsing the input file by constructing explicit and implicit geometric representations and performing quadtree decomposition. The quadtree meshes are used to classify blocks and calculate the intersection points information. Thirdly, extracting the intersection points information of the above blocks at the geometric boundary, new NURBS information is constructed with the help of the control points updating strategy proposed in Section 3.2 and 3.3, and the original geometric boundary is replaced with the aforementioned NURBS curves to construct a new quadtree meshes. Fourthly, the stiffness matrix of six internal elements is pre-calculated, and the element stiffness matrix for each element, including boundary elements, is determined. Subsequently, the overall stiffness matrix is assembled. Building upon this foundation, the finite element equilibrium equation is solved by determining loading and boundary conditions. Finally, the NURBS-boundary-based quadtree scaled boundary finite element method is realized, and the required displacement and stress are obtained. The implementation flow chart of NQSBFEM is shown in Fig. 17.

5. Numerical examples

5.1. Example 1

This example serves primarily to validate the rationality of the proposed NURBS-boundary-based SBFEM. Assume a curve boundary element and its size information under quadtree decomposition, as shown in Fig. 18.

The element is analyzed utilizing the four methodologies illustrated in Fig. 19. Fig. 19(a) exhibits solution of the NURBS-boundary-based SBFEM. Where the coordinates of the control point (red circle) of the NURBS boundary are [0.5 0.5; 0 1; −0.5 0.5](mm), the knot vector is [0 0 0 1 1 1], and the corresponding weight is $[1\ \sqrt{2}/2\ 1]$, the degree is set to 2. The remaining node coordinates are [−0.5 0.5; −0.5 −0.5; 0.5 −0.5; 0.5 0.5] (mm), with the notable observation that the starting and ending control points of the NURBS curve fall exactly on the element node. The force with a magnitude of 10 N are applied to the left and right tips of the element, while the left and right bottom ends are fixed. The elastic modulus is set at 1000 Mpa, and Poisson's ratio is 0.3. Additionally, the analysis concept of HQSBFEM is introduced, which establishes a linear connection between node and node of boundary element, as illustrated in Fig. 19(b). In order to facilitate a more comprehensive

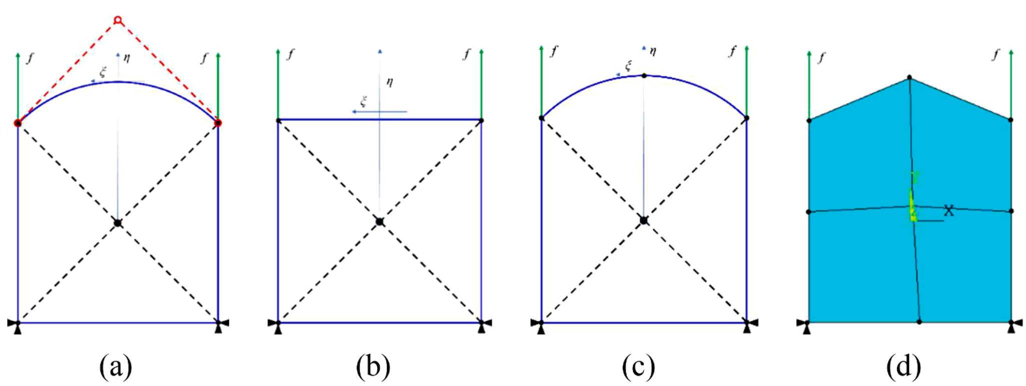

Fig. 19. Curve boundary element, (a) NURBS-boundary, (b) linear boundary, (c) quadratic boundary, (d) FEM.

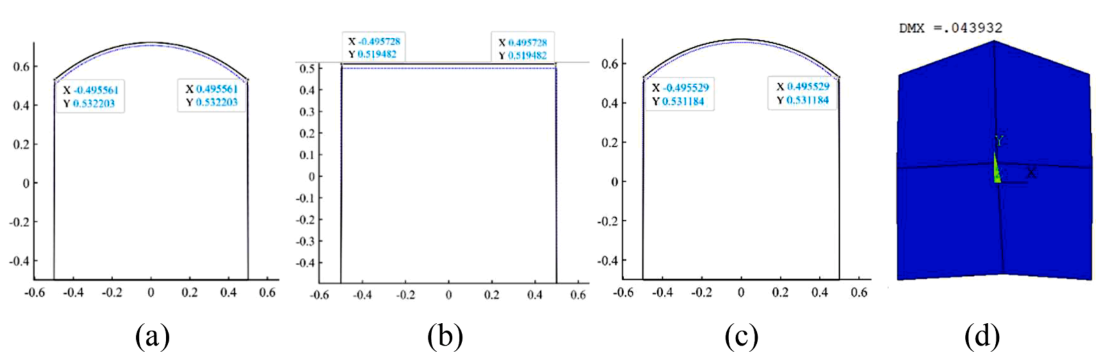

Fig. 20. The deformed boundary element, (a) NURBS-boundary, (b) linear boundary, (c) quadratic boundary, (d) FEM.

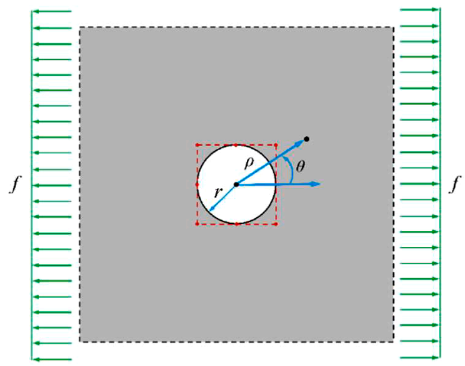

Fig. 21. Infinite plane with hole.

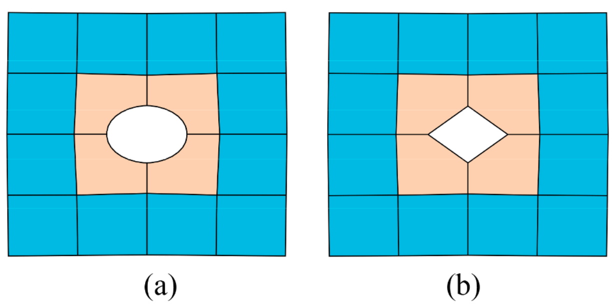

Fig. 22. Structural quadtree deformed mesh, (a) NQSBFEM, (b) HQSBFEM.

comparison, the polygon SBFEM of the quadratic curve boundary is utilized to analyze the aforementioned element, as depicted in Fig. 19(c). And Fig. 19(d) shows the solution of the finite element software when the boundary element is discretized into four elements.

The deformed boundary elements corresponding to Fig. 19 are shown in Fig. 20. The maximum node displacements of NURBS-boundary, linear boundary and quadratic boundary are 0.0325 mm, 0.0199 mm and 0.0312 mm respectively. Where the blue dashed mesh represents the initial element while the black mesh depicts the deformed element. Furthermore, the NURBS-boundary node displacement is more similar to the displacement 0.04392 mm when the finite element software divides multiple meshes, indicating that the proposed method is more advantageous.

5.2. Example 2

The purpose of this example is to validate the applicability of NQSBFEM. Fig. 21 illustrates an infinite plane with hole under remote uniaxial uniform tension $f = 1$ N. The circular hole is represented by a NURBS curve, with a radius of 0.5 mm and control points (red points) at [0.5 0; 0.5 −0.5; 0 −0.5; −0.5 −0.5; −0.5 0; −0.5 0.5; 0 mm 0.5; 0.5 0.5; 0.5 0] (mm). The knot vector is [0 0 0 1/4 1/4 2/4 2/4 3/4 3/4 1 1 1], the weight are [1 $\sqrt{2}/2$ 1 $\sqrt{2}/2$ 1 $\sqrt{2}/2$ 1 $\sqrt{2}/2$ 1], and the degree is set to 2. The elastic modulus is defined as1000 MPa and Poisson's ratio as $\mu = 0.3$. Computation is performed on a PC with 12th Gen Intel(R) Core (TM) i7–12700F 2.10 GHz CPU and 16 GB RAM.

A square of dimension 4 × 4 is employed around the circular hole instead of the infinite plane to model, and the displacement's exact solution is specified as the boundary conditions for all four sides of the square. The exact solution for this problem in polar coordinates (ρ, θ) [41] is provided as follows

$$\begin{aligned} u_x &= \frac{fr}{8G}\left[\frac{\rho}{r}(1+\kappa)\cos\theta + \frac{2\rho}{r}((1+\kappa)\cos\theta + \cos 3\theta) - \frac{2\rho^3}{r^3}\cos 3\theta\right] \\ u_y &= \frac{fr}{8G}\left[\frac{\rho}{r}(\kappa-3)\sin\theta + \frac{2\rho}{r}((1-\kappa)\sin\theta + \sin 3\theta) - \frac{2\rho^3}{r^3}\sin 3\theta\right] \end{aligned} \tag{38}$$

where G is the shear modulus and κ is Kolosov constant, defined as

$$\kappa = \begin{cases} \dfrac{3-\mu}{1+\mu} \text{ for plane stress} \\ 3-4\mu \text{ for plane strain} \end{cases} \tag{39}$$

When both the inner and outer boundary seed points are set to 4, Fig. 22 illustrates the quadtree deformation of NQSBFEM and HQSBFEM. It can be observed intuitively that in Fig. 22(a), the inner boundary retains its circular characteristics, with the orange element representing the boundary element, which can be addressed using the method described in Section 3.4. Conversely, Fig. 22(b) exhibits a diamond-shaped structure, which obviously loses the basic characteristic of a circle and inevitably introduces significant errors. In this context, further mesh refinement is required.

In order to further investigate the impact of mesh refinement on the results, the structural deformation under the aforementioned methods

Table 1
Comparison of quadtree deformed mesh under different smallest sub-cell level.

Sub-cell level	2^6	2^5	2^4	2^3
NQS BFEM	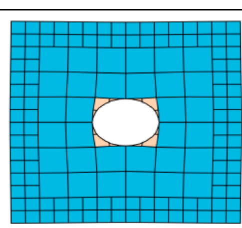	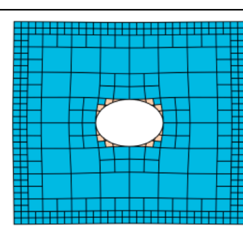	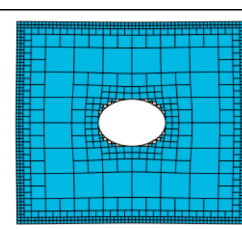	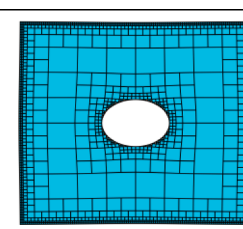
HQS BFEM	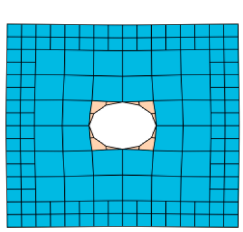	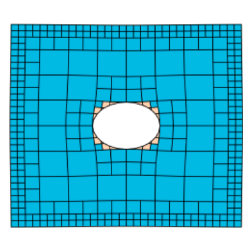	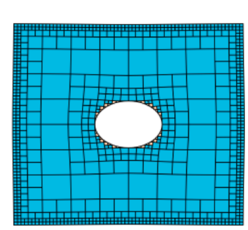	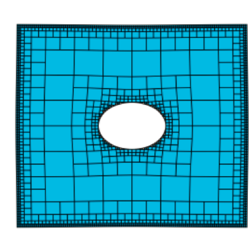

Table 2
The relationship between the relative displacement error norm, time, the numbers of element and DOFs.

Element numbers	DOFs		N_{rde}		Time(s)	
	NQS BFEM	HQS BFEM	NQS BFEM	HQS BFEM	NQS BFEM	HQS BFEM
16	72	56	0.01658	0.04101	0.08022	0.08000
156	464	400	0.00684	0.01428	0.10425	0.10222
380	1104	976	0.00397	0.00633	0.11351	0.10899
860	2448	2192	0.00229	0.00308	0.15219	0.14384
1780	5056	4544	0.00192	0.00239	0.23511	0.20799

are presented in the Table 1 when using a seed number of 130 for the inner boundary and 39 for the outer boundary, along with smallest sub-cell level of 2^6, 2^5, 2^4, and 2^3. It is evident that even with continuous mesh refinement, NQSBFEM can successfully perform the corresponding calculations, thereby demonstrating its excellent applicability and consistently yielding smooth boundaries. Different from literature [25], the proposed method enables the adaptive updating of NURBS information in response to changes in the quadtree mesh, thus avoiding manual insertion of new NURBS information. Furthermore, HQSBFEM tends to exhibit smoother inner boundaries as a result of mesh refinement.

For the purpose of error estimation and convergence research, the relative displacement error norm N_{rde} is utilized for verification. Its mathematical expression is as follows

$$N_{rde} = \frac{\| \boldsymbol{u}^{exa} - \boldsymbol{u}^{h} \|}{\boldsymbol{u}^{exa}} \tag{40}$$

where $\boldsymbol{u}^{exa}$ and $\boldsymbol{u}^{h}$ represent the analytical solution and the numerical solution, respectively. Under the case of 5 kinds of mesh division, the relationship between the relative displacement error norm, time (including pre-processing + analysis solution), the numbers of element and degree of freedom (DOF) are shown in the Table 2. Fig. 23 shows the corresponding comparison curve of the table.

By combining the Table 2 and the Fig. 23, it can be observed that as the mesh is continuously subdivided, the relative displacement error norm under NQSBFEM and HQSBFEM gradually decreases, indicating a convergence trend. The former exhibits smaller N_{rde} values under the same number of elements, suggesting superior analytical accuracy. Moreover, as the number of DOFs increases, both methods experience an increase in computation time. The NURBS boundary of NQSBFEM is augmented with additional control points, depicted as blue asterisks in Fig. 24, resulting in a corresponding increase in its solution time, where the red circle is the control point on the node. Nevertheless, for the case with 2448 DOF, NQSBFEM achieves better N_{rde} than HQSBFEM with 4544 DOF. Specifically, the former requires 26.8 % less computation time compared to the latter. In other words, NQSBFEM can achieve higher computational accuracy with fewer mesh divisions while saving time and cost.

5.3. Example 3

This example presents a simplistic petal structure for stress analysis. The design domain of the petal structure is depicted in Fig. 25, where the boundary of the circle is represented by a NURBS curve. The control points are located at coordinates [2 0; 2 1; 1 1; 1 2; 0 2; −1 2; −1 1; −2 1;

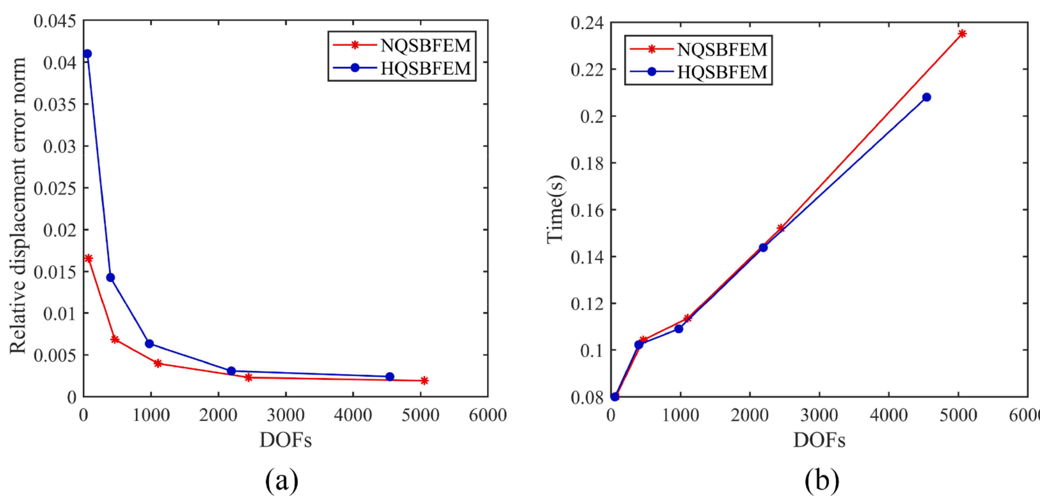

Fig. 23. Comparison curves between NQSBFEM and HQSBFEM, (a) relative displacement error norm, (b) time.

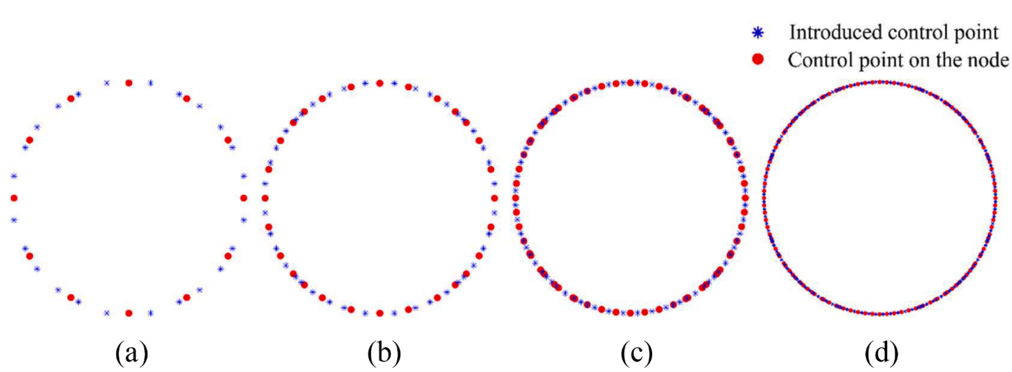

Fig. 24. Schematic diagram of NURBS control points under different mesh divisions, (a) 156, (b) 380, (c) 860, (d) 1780.

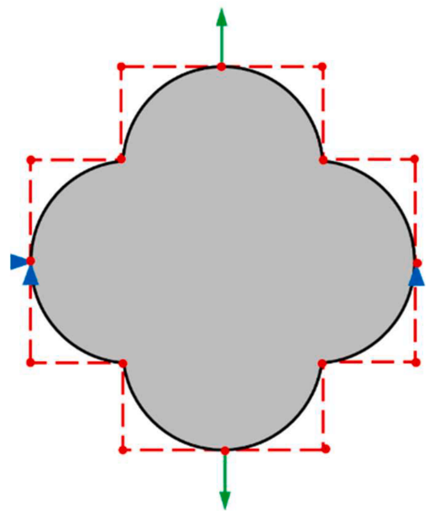

Fig. 25. Schematic diagram of petal structure.

Table 3
Boundary elements number, total elements number and maximum von-Mises stress values under HQSBFEM, NQSBFEM and FEM.

	Boundary elements	Total elements	Maximum stress (MPa)
HQSBFEM	248	507	14.3843
NQSBFEM	248	507	16.2147
FEM	248	3803	18.7005

−2 0; −2 −1; −1 −1; −1 −2; 0 −2; −1 −2; 1 −1; 2 −1; 2 0] (mm). The knot vector is defined as [0 0 0 1/8 1/8 2/8 2/8 3/8 3/8 4/8 4/8 5/8 5/8 6/8 6/8 7/8 7/8 1 1 1], the weights are [1 $\sqrt{2}/2$ 1 $\sqrt{2}/2$ 1 $\sqrt{2}/2$ 1 $\sqrt{2}/2$ 1 $\sqrt{2}/2$ 1 $\sqrt{2}/2$ 1 $\sqrt{2}/2$ 1 $\sqrt{2}/2$ 1], and the degree is set to 2. A load of magnitude 100 N is applied to both the top and bottom of the petal structure. The left end is fixed, while the right end is only fixed in the Y-axis direction. The modulus of elasticity is specified as 1000 MPa and Poisson's ratio is set at 0.3.

The basic settings of the quadtree are as follows: the size is set to $2^{10} = 1024$, the level of largest sub-cell is limit to $2^9 = 512$, and the level of smallest sub-cell is limit to $2^3 = 8$. When setting the seed points of the boundary at 120, Table 3 displays boundary elements number, total elements number and maximum von-Mises stress values under HQSBFEM and NQSBFEM. Figs. 26 and 27 illustrate the corresponding mesh division and stress distribution. Additionally, we also analyze the petal structure with the assistance of finite element software, in order to achieve a better comparison effect, so that the number of boundary elements after the mesh division is equal to the number of elements in the quadtree decomposition, both are 248.

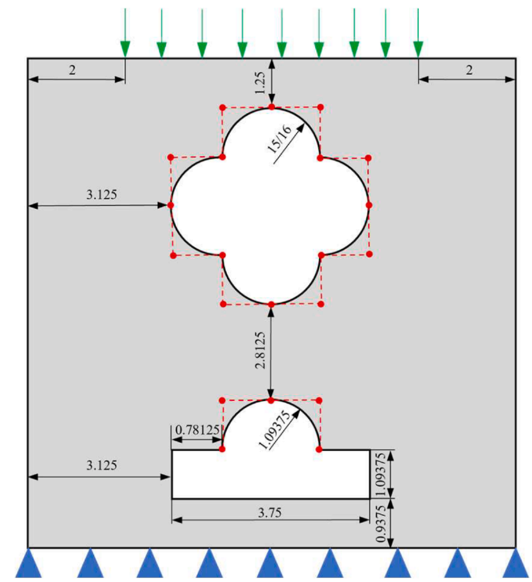

Fig. 28. Square plate with two irregular holes.

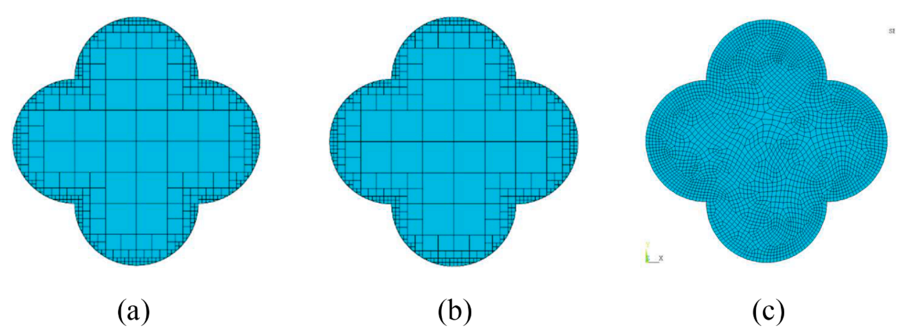

Fig. 26. Divided mesh diagram, (a) HQSBFEM, (b) NQSBFEM, (c) FEM.

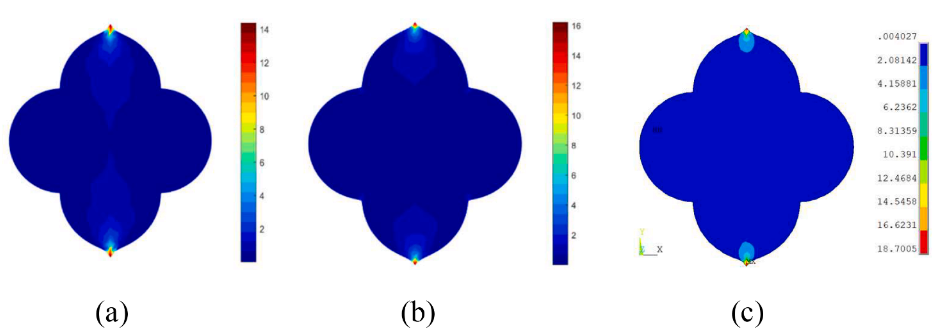

Fig. 27. Von-Mises stress distribution diagram, (a) HQSBFEM, (b) NQSBFEM, (c) FEM.

Table 4
The relationship between the element numbers, DOFs, maximum von-Mises stress values and time.

	Element numbers	DOFs	Maximum stress (MPa)	Time(s)
NQSBFEM	699	2254	7.22	0.15198
HQSBFEM	699	2016	6.32	0.14297
HQSBFEM	1497	4240	7.17	0.20562

It can be observed from the stress diagram that despite having an equal number of boundary elements, there are more meshes divided by finite element software resulting in larger stress values obtained. The maximum stress value obtained by NQSBFEM under similar mesh divisions surpasses that obtained by HQSBFEM but aligns more closely with results from finite element software analysis. In addition, the stress values at the four corners of NQSBFEM are comparatively higher when compared to the other two methods. This can be attributed to employing NURBS curves on boundaries along with high-order continuity between elements, which leads to stress results that are more consistent with

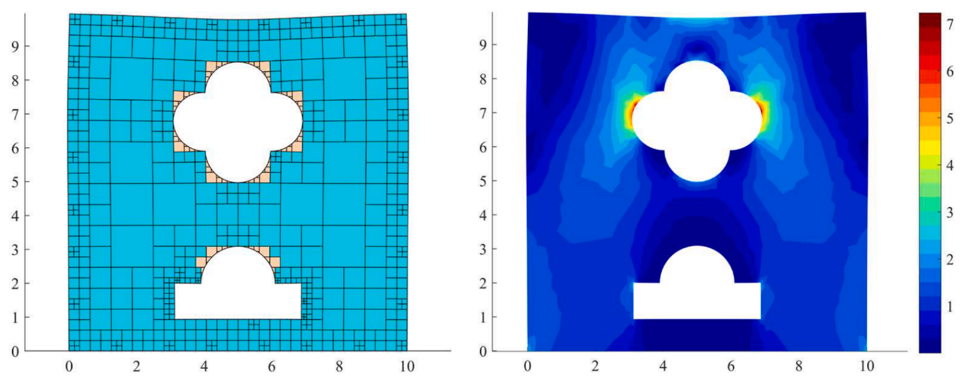

(a) (b)

Fig. 29. Schematic diagram of NQSBFEM with 699 elements, (a) Quadtree deformed mesh, (b) Von-Mises stress.

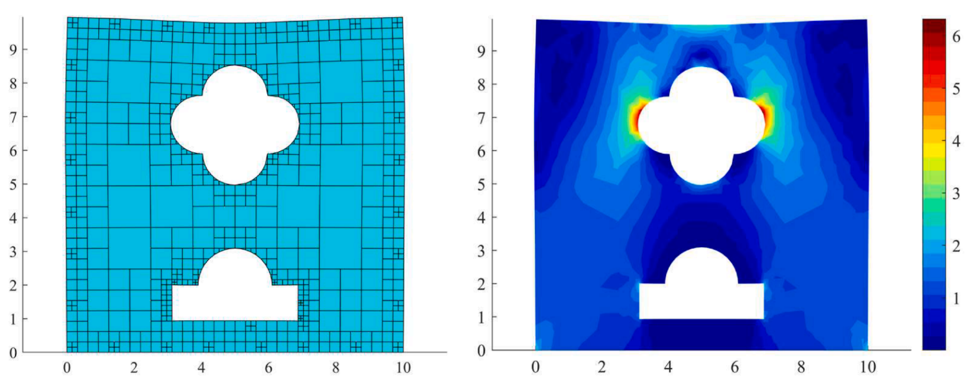

(a) (b)

Fig. 30. Schematic diagram of HQSBFEM with 699 elements, (a) Quadtree deformed mesh, (b) Von-Mises stress.

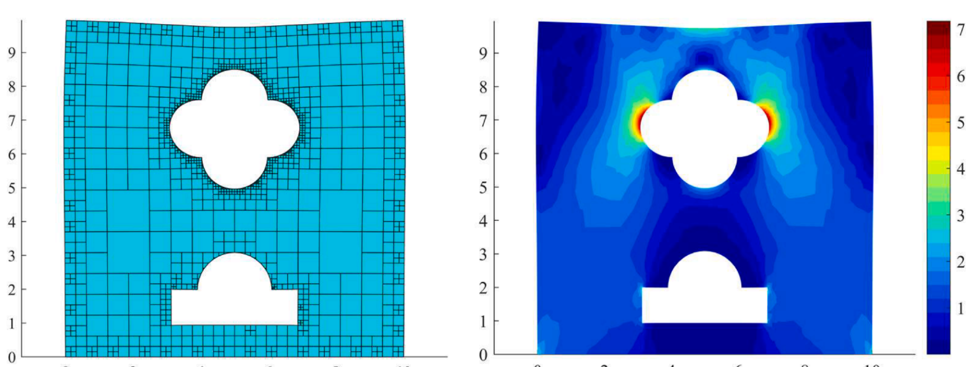

(a) (b)

Fig. 31. Schematic diagram of HQSBFEM with 1497 elements, (a) Quadtree deformed mesh, (b) Von-Mises stress.

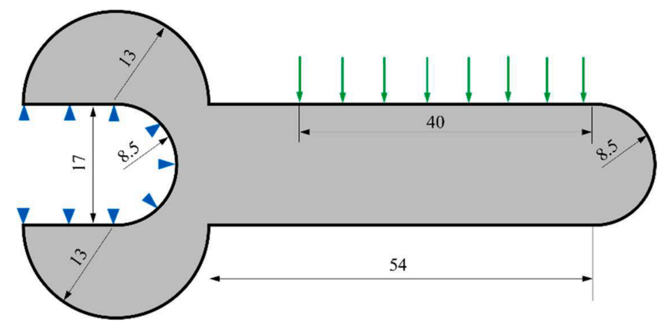

Fig. 32. Wrench structure and its size information.

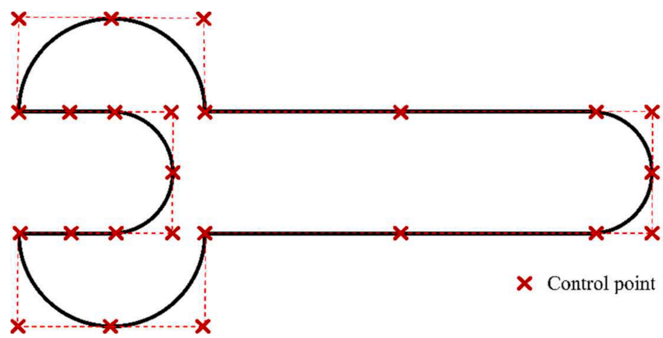

Fig. 33. Control points of wrench structure.

physical laws.

5.4. Example 4

This example provides a square plate with two irregular holes to measure the efficiency and result accuracy of the NQSBFEM. The side length of the plate is 10 mm. A uniform load of 1 N/mm is applied to [2, 8] segment of the upper boundary, the lower boundary is fixed, and the dimensions and control points of the holes are shown in Fig. 28. The modulus of elasticity is specified as 1000 MPa and Poisson's ratio is set at 0.3.

Table 4 displays element numbers, DOFs, maximum von-Mises stress values and time under HQSBFEM and NQSBFEM. The corresponding quadtree deformed meshes and Von-Mise stress diagrams are displayed in Figs. 29-31.

When the number of divided elements is 699, NQSBFEM demonstrates superior stress performance compared to HQSBFEM, despite the time increase caused by the introduction of additional control points. The stress performance of HQSBFEM approaches that of NQSBFEM with low mesh division when the number of divided elements is 1497, and the time consumed by HQSBFEM is 0.20562. Specifically, the NQSBFEM requires 26.1 % less computation time compared to the HQSBFEM, indicating that former achieves higher computational accuracy with fewer mesh divisions while saving time.

5.5. Example 5

This example provides a wrench structure for analysis and the size information is illustrated in Fig. 32. The groove of the wrench head remains fixed while uniform load of 0.025 N/mm is applied to the handle. The control points of wrench structure are presents in Fig. 33, and the degree is set to 2. The modulus of elasticity is specified as 1000 MPa and Poisson's ratio is set at 0.3.

The Von-Mises stress diagram of the wrench structure under NQSBFEM is presented in Fig. 34(a), where the maximum stress value is 0.3202 with a total of 591 divided elements under quadtree decomposition. In comparison, Fig. 34(b) displays the Von-Mises stress diagram under finite element software with a mesh consisting of 22,251 elements. It can be observed that NQSBFEM achieves superior analysis accuracy while utilizing fewer mesh divisions.

6. Conclusions

This paper proposes a NURBS-boundary-based quadtree SBFEM, which enables efficient and rapid solution of irregular design domain. Specifically, the mesh is divided using quadtree decomposition, while SBFEM effectively addresses the issue of hanging nodes in the quadtree mesh. Simultaneously, due to the accurate representation of structural boundaries by NURBS curves, there is no necessity for detailed mesh subdivision within the design domain, ultimately resulting in a reduction of time spent on such division. Numerical examples demonstrate the capability of proposed method to achieve adaptive meshing and generate NURBS curves for subsequent solution. In comparison with the conventional hybrid quadtree SBFEM, this method successfully fulfills expectations in terms of displacement and stress. Furthermore, the method exhibits significant potential in addressing challenges such as fracture, heat conduction, and dynamics. However, there still exist obstacles concerning the geometric description and solution of plates, shells, and especially thin-walled cylinders. Moving forward, the focus of our research will be on exploring novel approaches to address the aforementioned challenges, as well as investigating efficient and high-

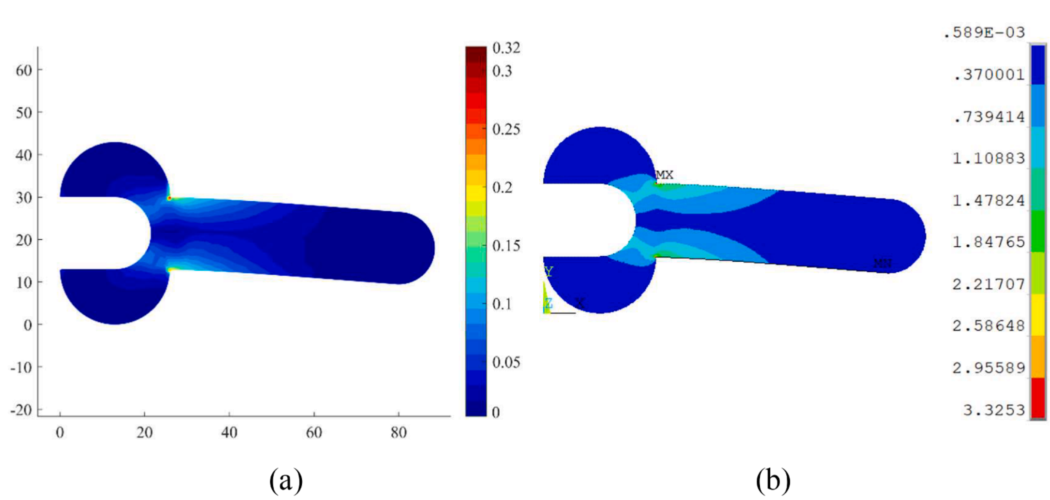

Fig. 34. Von-Mises stress distribution diagram, (a) HQSBFEM, (b) FEM.

precision solutions for three-dimensional solid structures in conjunction with the aforementioned research.

CRediT authorship contribution statement

Xinqing Li: Investigation, Methodology, Software, Validation, Writing – original draft. **Hailiang Su:** Methodology, Validation. **Jianghong Yang:** Methodology, Software. **Guifeng Gao:** Methodology, Software. **Yingjun Wang:** Methodology, Software, Validation, Writing – review & editing.

Declaration of Competing Interest

The authors declare that they have no known competing financial interests or personal relationships that could have appeared to influence the work reported in this paper.

Data availability

Data will be made available on request.

Acknowledgements

This work has been supported by National Natural Science Foundation of China [No. 52075184]. This support is gratefully acknowledged.

References

[1] Cottrell JA, Hughes TJR, Bazilevs Y. Isogeometric analysis: toward integration of CAD and FEA. Wiley & Sons; 2009. https://doi.org/10.1002/9780470749081.ch1.
[2] Klinkel S, Chen L, Dornisch W. A NURBS based hybrid collocation–Galerkin method for the analysis of boundary represented solids. Comput Methods Appl Mech Eng 2015;284:689–711. https://doi.org/10.1016/j.cma.2014.10.029.
[3] Song C, Wolf JP. The scaled boundary finite-element method—alias consistent infinitesimal finite-element cell method—for elastodynamics. Comput Methods Appl Mech Eng 1997;147:329–55. https://doi.org/10.1016/S0045-7825(97)00021-2.
[4] Samet H. The quadtree and related hierarchical data structures. ACM Comput Surv 1984;16:187–260. https://doi.org/10.1145/356924.356930.
[5] Greaves DM, Borthwick AGL. Hierarchical tree-based finite element mesh generation. Int J Numer Methods Eng 1999;45:447–71. 10.1002/(SICI)1097-0207(19990610) 45:4 <447::AID−NME592>3.0.CO; 2-%23.
[6] Reddy P, Montas HJ, Samet H, Shirmohammadi A. Quadtree-based triangular mesh generation for finite element analysis of heterogeneous spatial data. ASAE Ann Int Meet 2001;300:1–25.
[7] Tabarraei A, Sukumar N. Adaptive computations on conforming quadtree meshes. Finite Elem Anal Des 2005;41:686–702. https://doi.org/10.1016/j.finel.2004.08.002.
[8] Gravenkamp H, Duczek S. Automatic image-based analyses using a coupled quadtree-SBFEM/SCM approach. Comput Mech 2017;60:559–84. https://doi.org/10.1007/s00466-017-1424-1.
[9] H. Man, C. Song, S. Natarajan, E.T. Ooi, C. Birk, Towards automatic stress analysis using scaled boundary finite element method with quadtree mesh of high-order elements, ArXiv e-prints, 2014, math.NA/1402.5186. https://doi.org/10.48550/arXiv.1402.5186.
[10] Ooi ET, Man H, Natarajan S, Song C. Adaptation of quadtree meshes in the scaled boundary finite element method for crack propagation modelling. Eng Fract Mech 2015;144:101–17. https://doi.org/10.1016/j.engfracmech.2015.06.083.
[11] Ooi ET, Natarajan S, Song C, Ooi EH. Dynamic fracture simulations using the scaled boundary finite element method on hybrid polygon–quadtree meshes. Int J Impact Eng 2016;90:154–64. https://doi.org/10.1016/j.ijimpeng.2015.10.016.
[12] Ooi ET, Natarajan S, Song C, Ooi EH. Crack propagation modelling in concrete using the scaled boundary finite element method with hybrid polygon–quadtree meshes. Int J Fract 2017;203:135–57. https://doi.org/10.1007/s10704-016-0136-4.
[13] Song C, Ooi ET, Pramod ALN, Natarajan S. A novel error indicator and an adaptive refinement technique using the scaled boundary finite element method. Eng Anal Bound Elem 2018;94:10–24. https://doi.org/10.1016/j.enganabound.2018.05.010.
[14] Chen X, Luo T, Ooi ET, Ooi EH, Song C. A quadtree-polygon-based scaled boundary finite element method for crack propagation modeling in functionally graded materials. Theor Appl Frac Mec 2018;94:120–33. https://doi.org/10.1016/j.tafmec.2018.01.008.
[15] Yu B, Hu P, Saputra AA, Gu Y. The scaled boundary finite element method based on the hybrid quadtree mesh for solving transient heat conduction problems. Appl Math Model 2021;89:541–71. https://doi.org/10.1016/j.apm.2020.07.035.
[16] Gravenkamp H, Saputra AA, Song C, Birk C. Efficient wave propagation simulation on quadtree meshes using SBFEM with reduced modal basis. Int J Numer Methods Eng 2017;110:1119–41. https://doi.org/10.1002/nme.5445.
[17] Saputra A, Talebi H, Tran D, Birk C, Song C. Automatic image-based stress analysis by the scaled boundary finite element method, Internat. J Numer Methods Eng 2017;109:697–738. https://doi.org/10.1002/nme.5304.
[18] Guo H, Ooi ET, Saputra AA, Yang Z, Natarajan S, Ooi EH, Song C. A quadtree-polygon-based scaled boundary finite element method for image-based mesoscale fracture modelling in concrete. Eng Fract Mech 2019;211:420–41. https://doi.org/10.1016/j.engfracmech.2019.02.021.
[19] Zhang Z, Guo J, Zhang Z, Song X. Mesoscale damage modelling of concrete by using image-based scaled boundary finite element method. Int J Damage Mech 2021;30:1281–311. https://doi.org/10.1177/1056789521998414.
[20] Hughes TJR, Cottrell JA, Bazilevs Y. Isogeometric analysis: CAD, finite elements, NURBS, exact geometry and mesh refinement. Comput Methods Appl Mech Eng 2005;194:4135–95. https://doi.org/10.1016/j.cma.2004.10.008.
[21] Nguyen VP, Anitescu C, Bordas SPA, Rabczuk T. Isogeometric analysis: an overview and computer implementation aspects. Math Comput Simul 2015;117:89–116. https://doi.org/10.1016/j.matcom.2015.05.008.
[22] Wang Y, Xiao M, Xia Z, Li P, Gao L. From computer-aided design (CAD) toward human-aided design (HAD): an isogeometric topology optimization approach. Engineering 2023;22:94–105. https://doi.org/10.1016/j.eng.2022.07.013.
[23] Zhang Y, Lin G, Hu Z. Isogeometric analysis based on scaled boundary finite element method. IOP Conf Ser: Mater Sci Eng 2010;10:012237. https://doi.org/10.1088/1757-899X/10/1/012237.
[24] Lin G, Zhang Y, Hu Z, Zhong H. Scaled boundary isogeometric analysis for 2D elastostatics. Sci China Phys Mech 2014;57:286–300. https://doi.org/10.1007/s11433-013-5146-x.
[25] Zang Q, Bordas SPA, Liu J, Natarajan S. NURBS-Enhanced polygonal scaled boundary finite element method for heat diffusion in anisotropic media with internal heat sources. Eng Anal Bound Elem 2023;148:279–92. https://doi.org/10.1016/j.enganabound.2022.12.028.
[26] Reichel R, Klinkel S. A non-uniform rational B-splines enhanced finite element formulation based on the scaled boundary parameterization for the analysis of heterogeneous solids. Int J Numer Methods Eng 2023;124:2068–92. https://doi.org/10.1002/nme.7202.
[27] Natarajan S, Wang J, Song C, Birk C. Isogeometric analysis enhanced by the scaled boundary finite element method. Comput Methods Appl Mech Eng 2015;283:733–62. https://doi.org/10.1016/j.cma.2014.09.003.
[28] Xue B, Lin G, Hu Z. Scaled boundary isogeometric analysis for electrostatic problems, Engineering. Eng Anal Bound Elem 2017;85:20–9. https://doi.org/10.1016/j.enganabound. 2017.09.012.
[29] Liu J, Li J, Li P, Lin G, Xu T, Chen L. New application of the isogeometric boundary representations methodology with SBFEM to seepage problems in complex domains. Comput Fluids 2018;174:241–55. https://doi.org/10.1016/j.compfluid.2018.08.004.
[30] Yang YB, Li J. 2.5D prediction of soil vibrations due to railway loads by the isogeometric analysis with scaled boundary. Eng Anal Bound Elem 2022;134:341–59. https://doi.org/10.1016/j. enganabound.2021.10.012.
[31] Vuong AV, Giannelli C, Jüttler B, Simeon B. A hierarchical approach to adaptive local refinement in isogeometric analysis. Comput Methods Appl Mech Eng 2011;200:3554–67. https://doi.org/10.1016/j.cma.2011.09.004.
[32] Wu Z, Huang Z, Liu Q, Zuo B. A local solution approach for adaptive hierarchical refinement in isogeometric analysis. Comput Methods Appl Mech Eng 2015;283:1467–92. https://doi.org/10.1016/j.cma.2014.10.026.
[33] Bazilevs Y, Calo VM, Cottrell JA, Evans JA, Hughes TJR, Lipton S, Scott MA, Sederberg TW. Isogeometric analysis using T-splines. Comput Methods Appl Mech Eng 2010;199:229–63. https://doi.org/10.1016/j.cma.2009.02.036.
[34] Nguyen-Thanh N, Kiendl J, Nguyen-Xuan H, Wüchner R, Bletzinger KU, Bazilevs Y, Rabczuk T. Rotation free isogeometric thin shell analysis using PHT-splines. Comput Methods Appl Mech Eng 2011;200:3410–24. https://doi.org/10.1016/j.cma.2011.08.014.
[35] Piegl L, Tiller W. The NURBS book. Springer Science & Business Media; 1996.
[36] Wang YJ, Benson DJ. Multi-patch nonsingular isogeometric boundary element analysis in 3D. Comput Methods Appl Mech Eng 2015;293:71–91. https://doi.org/10.1016/j.cma.2015.03.016.
[37] Wolf JP, Song C. The scaled boundary finite-element method – a primer: derivations. Comput Struct 2000;78:191–210. https://doi.org/10.1016/S0045-7949(00)00099-7.
[38] Wolf JP, Song C. The scaled boundary finite-element method – a fundamental solution-less boundary-element method. Comput Methods Appl Mech Eng 2001;190:5551–68. https://doi.org/10.1016/S0045-7825(01)00183-9.
[39] Song C. A matrix function solution for the scaled boundary finite-element equation in statics. Comput Methods Appl Mech Eng 2004;193:2325–56. https://doi.org/10.1016/j.cma.2004.01.017.
[40] Song C. The scaled boundary finite element method: introduction to theory and implementation. John Wiley & Sons; 2018.
[41] Fries TP. Higher-order meshing of implicit geometries - part III. Conformal decomposition FEM (CDFEM). ArXiv; 2017. https://doi.org/10.48550/arXiv.1706.00919. abs/1706.00919.